

## A Study of Fast Flareless Coronal Mass Ejections

H. Q. SONG<sup>1,3</sup>, Y. CHEN<sup>1</sup>, D. D. Ye<sup>1</sup>, G. Q. HAN<sup>1</sup>, G. H. Du<sup>1</sup>, G. LI<sup>2,1</sup>, J. ZHANG<sup>3</sup>, AND Q. HU<sup>2</sup>

*1 Institute of Space Sciences and School of Space Science and Physics, Shandong University, Weihai, Shandong 264209, China*

yaochen@sdu.edu.cn

*2 Department of Physics and CSPAR, University of Alabama in Huntsville, Huntsville, AL 35899, USA*

*3 School of Physics, Astronomy and Computational Sciences, George Mason University, Fairfax, Virginia 22030, USA*

### ABSTRACT

Two major processes have been proposed to convert the coronal magnetic energy into the kinetic energy of a coronal mass ejection (CME): resistive magnetic reconnection and ideal macroscopic magnetohydrodynamic instability of magnetic flux rope. However, it remains elusive whether both processes play a comparable role or one of them prevails during a particular eruption. To shed light on this issue, we carefully studied energetic but flareless CMEs, *i.e.*, fast CMEs not accompanied by any flares. Through searching the Coordinated Data Analysis Workshops (CDAW) database of CMEs observed in Solar Cycle 23, we found 13 such events with speeds larger than  $1000 \text{ km s}^{-1}$ . Other common observational features of these events are: (1) none of them originated in active regions; they were associated with eruptions of well-developed long filaments in quiet-Sun regions, (2) no apparent enhancement of flare emissions was present in soft X-ray, EUV and microwave data. Further studies of two events reveal that (1) the reconnection electric fields, as inferred from the product of the separation speed of post-eruption ribbons and the photospheric magnetic field measurement, were in general weak; (2) the period with a measurable reconnection electric field is considerably shorter than the total filament-CME acceleration time. These observations indicate that, for these fast CMEs, the magnetic energy was released mainly via the ideal flux rope instability through the work done by the large scale Lorentz force acting on the rope currents rather than via magnetic reconnections. We also suggest that reconnections play a less important role in accelerating CMEs in quiet Sun regions of weak magnetic field than those in active regions of strong magnetic field.

*Subject headings:* instabilities – magnetic reconnection – Sun: coronal mass ejections (CME) – Sun: flares

## 1. Introduction

Coronal mass ejections (CMEs) are the most energetic eruptions in the solar system. Previous studies have established that many CMEs are accompanied by flares and some of the physical properties of CMEs and flares are closely related. For example, early investigations using the Solar Maximum Mission (SMM) data showed that about 48% of CMEs were accompanied by X-ray flares (Harrison 1995). The actual flare-accompanying rate could be higher than 90% if considering the fact that nearly half of the observed CMEs were from the back side of the Sun. Later studies revealed good correlations between CME speed (acceleration) profiles with the soft X-ray (hard X-ray and microwave) profiles of associated flares (e.g., Zhang et al. 2001; Qiu et al. 2004; Maričić et al. 2007). In addition, the CME acceleration was also found to be related to the inferred reconnection electric fields (Qiu et al. 2004). Studies of connecting the extrapolated magnetic flux in the flaring region to the magnetic flux of the flux rope reconstructed from in-situ data showed that the two fluxes were comparable (Qiu et al. 2007). These CME-flare association studies strongly suggest an important role played by magnetic reconnections in energizing CMEs.

Nevertheless, there are also studies indicating that in some events CMEs and flares are only loosely connected. For instance, it is well known that there exist CMEs without accompanying flares or only associated with hardly-recognizable flares (e.g., Gosling et al., 1976; Sheeley et al. 1999). On the other hand,  $\sim 70\%$  of C-level, 44% of M-level, and 10% of X-level flares are not associated with CMEs according to recent statistical studies (Yashiro et al. 2005; Wang and Zhang 2007). In addition, statistical studies with a large sample of events showed that the projected speed and kinetic energy of CMEs were only weakly correlated with the peak values of soft X-ray flux (e.g., Yashiro et al. 2002; Vršnak et al. 2005; see also Hundhausen (1997) for an earlier study). After correcting the projection effect, the correlation became even weaker (Yeh et al. 2005). An explanation to these observations is that there exist other important factors affecting the energy release process of CMEs besides magnetic reconnection (e.g., Chen 2011). It should be noted that in many studies magnetic reconnections were suggested to be the essential energizing process of CMEs. This suggestion was often based on the CME-flare synchronization and the evolutionary similarity of specific physical quantities of the two phenomena, rather than on the ground of direct cause-effect analysis.

Theoretically, it is well known that in the corona there exist two important magnetic energy release mechanisms, one is the magnetic reconnection, and the other the global magnetohydrodynamic (MHD) flux rope instability (e.g., Van Tend and Kuperus 1978; Priest and Forbes 1990; Forbes and Isenberg 1991; Isenberg et al. 1993; Forbes and Priest 1995; Hu et al. 2003; Kliem and Török 2006; Fan and Gibson 2007; Chen et al. 2007a, 2007b; Olmedo and Zhang, 2010). Via the later process the magnetic energy is converted into the kinetic energy mainly through the work done by the Lorentz force acting on the flux rope currents (c.f., Chen and Krall, 2003; Chen et al. 2006, 2007a). Along with the rising of the flux rope, a current sheet can be formed when field lines of opposite directions are pushed together. This provides favorable conditions for magnetic reconnection accounting for flares (Carmichael 1964; Sturrock 1966; Hirayama 1974; Kopp

& Pneuman 1976). Magnetic energy can be further released through reconnection to enhance the acceleration of the flux rope, giving rise to a feedback relationship between the CME dynamics and reconnection-induced processes (e.g., Zhang & Dere 2006; Maričić et al., 2007). Although this can explain the observed CME-flare correlations, it does not promise the importance of magnetic reconnection in CME energetics.

In a recent numerical simulation of CMEs, Chen et al. (2007a) modeled the flux rope eruption within the framework of ideal MHD. It was found that CMEs as fast as  $1000 \text{ km s}^{-1}$  can be produced even in the absence of magnetic reconnections. This point was supported by a later numerical modeling of flux rope eruption (Rachmeler et al. 2009). This naturally leads to a fundamental question for CME studies: which energy release mechanism dominates in a specific event, and what is the relative contribution of each mechanism if both are important? The majority existing studies focused on fast CMEs associated with flares from active regions. In this study, we draw attentions to a special group of fast yet flareless CMEs, trying to shed new light on the energizing process of CMEs.

## 2. Event identification and data analysis

The events of this study were selected through the online CDAW (Coordinated Data Analysis Workshops) database for CMEs observed by the Large Angle and Spectrometric Coronagraph (LASCO; Brueckner et al. 1995) on board the *Solar and Heliospheric Observatory (SOHO)* in Solar Cycle (SC) 23. We only considered front-side flareless CMEs with a linear speed greater than  $1000 \text{ km s}^{-1}$  and an angular width larger than  $20^\circ$ . The last condition is to exclude the fast narrow jet events which are considered to be physically different from normal CMEs (see, e.g., Chen, 2011). To ensure that the events are front-sided, we examined the simultaneous images given by the Extreme Ultraviolet Imaging Telescope (EIT, Delaboudiniere et al. 1995) on board *SOHO* to find clear eruptive signatures associated with the CME, like post-eruption loops, ribbons, or eruptive filaments. We require that these post-eruption signatures should be mostly observed in the EIT field of view (FOV) to make sure that any accompanying flare is not blocked by the solar disk. To determine the presence of accompanying flares, we back-extrapolated the CME start time assuming a constant propagation speed fixed at the corresponding CME linear speed measured with the LASCO data, and checked the GOES X-ray profile in a 6-hour time window centered at the obtained start time. If a flare was found in this period, we then verified its association with the CME using the EIT images and the flare timing and source location provided by the National Geophysical Data Center (NGDC) (<ftp://ftp.ngdc.noaa.gov/STP/space-weather/solar-data/>). Only CMEs without associated X-ray flares were included.

In total, we found 13 events conforming to the above conditions. Through analyzing the EIT movies and available pre-eruption  $H\alpha$  images, it was confirmed that all these events were associated with eruptive filaments in the quiet-Sun region. According to the magnetic field data given by the Michelson Doppler Imager (MDI; Scherrer et al. 1995), we found that in 5 events the filaments

were located above the neutral line inside a single extended bipolar region (EBR), while in the rest 8 events the filaments were located above the neutral region between two adjacent EBRs. We refer the former 5 events as Group A, and the rest 8 events as Group B. Similar classification method of CMEs based on their source magnetic field distributions has been adopted by Zhou et al. (2005, 2006).

In Table 1 we list the relevant parameters of the CMEs and filaments. The event number and group identification are given in the first column, the first appearance time of CME in the C2 FOV and the back-extrapolated CME start time are given in the second column. The third and fourth columns present the central position angle (CPA) and the angular width of the CMEs, the fifth and sixth columns show the projected linear speed and acceleration. The estimated CME mass and kinetic energy are included in the seventh and the eighth columns. All these data are taken from the CDAW database. In the last columns we show the central position and angular length of the pre-eruption filaments. These filament data are provided by the Paris observatory (<http://bass2000.obspm.fr/home.php>) except those for Events 1, 6, and 13 whose parameters were measured by the authors.

Table 1: Parameters of the 13 CMEs and associated filaments, see text for details.

Event#/ Group	CME							Filament	
	First C2 appearance time/CME start time (UT)	CPA (°)	Ang. Wid.(°)	Velocity (km s <sup>-1</sup> )	Acce. (m s <sup>-2</sup> )	Mass (g)	Ek (erg)	Center pos. (°)	Ang. length (°)
01/B	98/01/03 09:42/09:24	290	85	1020	21.8	2.8e15	1.4e31	N42W70	38
02/B	98/06/05 07:02/06:30	205	132	1017	28.3	–	–	S36W7	23
03/B	99/09/16 16:54/16:42	6	147	1021	49.3	–	–	N36W17	46
04/B	99/09/23 15:54/15:36	262	77	1150	-5.8	3.4e15	2.2e31	S23W41	22
05/B	00/07/24 16:54/16:29	220	50	1246	-48.7	3.2e15	2.4e31	S32W80	16
06/B	02/03/02 15:06/15:00	124	149	1131	5.4	–	–	S28E74	48
07/A	02/05/11 20:06/19:47	19	52	1003	5.4	1.1e15	5.5e30	N41E24	13
08/A	02/07/13 11:30/10:55	147	40	1037	-21.6	1.5e16	5.2e31	S31E28	18
09/A	02/08/06 18:25/17:35	218	134	1098	-0.5	–	–	S36W25	46
10/A	02/12/21 02:30/02:04	2	225	1072	-3.0	–	–	N40E9	24
11/B	02/12/26 18:30/18:07	80	24	1075	5.7	3.3e15	1.9e31	N14E73	7
12/A	03/01/05 10:37/09:52	353	67	1183	14.2	1.3e15	9.2e30	N39E17	17
13/B	05/01/04 09:30/09:14	288	102	1087	9.5	6.9e15	4.1e31	N8W58	31

It can be seen from Table 1 that the average width of all CMEs is  $\sim 100^\circ$ , and the angular width is less than  $50^\circ$  in only two events, the CME linear speeds distribute in a range of  $1003 - 1246 \text{ km s}^{-1}$  with an average of  $1088 \text{ km s}^{-1}$ , the acceleration varies between  $-48.7$  and  $49.3 \text{ m s}^{-2}$ . Estimates of the CME masses and kinetic energies are available from CDAW for 8 events. Among them, Event 8 (7) has the largest (smallest) mass and energy being  $1.5 \times 10^{16}$  ( $1.1 \times 10^{15} \text{ g}$ )

and  $5.2 \times 10^{31}$  ( $5.5 \times 10^{30}$ ) erg. The average values of the estimated CME masses and kinetic energies for these 8 events are  $4.63 \times 10^{15}$  g and  $2.33 \times 10^{31}$  erg,  $\sim 4$  and 12 times larger than the respective average values given by Webb et al. (2012) for all CMEs observed from 1996 to 2011. It should be pointed out that large errors are associated with these estimates of CME masses and energies. Nevertheless, it is reasonable to say that most of our events belong to relatively energetic ones among all CMEs. The filament length varies in a range of  $7^\circ - 48^\circ$  with an average of  $\sim 27^\circ$ . The filament CPAs distribute in a range of latitudes from S36 – N42.

In Figure 1 we present the radial variation of the projected speeds of CMEs for Group A observed by LASCO C2 and C3 (left panels), and the corresponding temporal evolution of the GOES X-ray flux (0.1 - 0.8 nm) in the 6-hour time window centered at the extrapolated CME start time (right panels). The corresponding profiles for the 8 events in Group B are shown in Figure 2. The CME speeds are given by the numerical differentiation using 3-point, Lagrangian interpolation. Note that the uncertainties of the CME speed and acceleration come mainly from the uncertainty in height measurements. The CME heights used here were measured by the authors. Their measurement errors are estimated to be 5 pixels in C2 and C3 images, corresponding to  $0.0625$  and  $0.2938 R_\odot$ , respectively. These errors are propagated in the standard way to estimate the errors of velocity and acceleration. The obtained speeds are not the same as that given by the CDAW database due to the measurement uncertainty. In general our speeds are slightly lower than those shown in CDAW. For example, the average of the linear speeds in all events becomes  $962 \text{ km s}^{-1}$ , and the speeds exceed  $1000 \text{ km s}^{-1}$  in only 5 events. In the rest 5 and 3 events, the linear speeds are in the range of  $900 - 1000 \text{ km s}^{-1}$  and  $800 - 900 \text{ km s}^{-1}$ , respectively. Despite this difference, all CMEs still belong to fast ones considering that the average speed of CMEs observed from 1996 - 2006 with an angular width larger than  $30^\circ$  was  $\sim 470 \text{ km s}^{-1}$  (Gopalswamy et al. 2009). Therefore, it will not change the result of this study.

In the 6-hour time window centered at the CME start time, there are 23 GOES X-ray flares recorded by NGDC. These flares have been listed in Table 2 of the Appendix, where we deduced that none of them may have contributed significantly to the acceleration of our CMEs, and thus are irrelevant to our study.

Comparing the left panels of Figures 1 and 2, we observe an obvious difference of CME speed profiles. For 4 events in Group A (except Event 10), the speeds keep almost constant or decline with distance. This indicates that most events of this group have finished the acceleration before entering into the C2 FOV ( $2 R_\odot - 6 R_\odot$ ). For 7 events in Group B (except Event 11), the speeds still increase significantly after entering into the C2 FOV, and reach their peaks around  $6 R_\odot - 9 R_\odot$ . Similar speed differences of the two groups are also present in the CDAW measurements. The group classifications stem from the magnetic sources of the eruptions. We therefore suggest that the observed speed evolutionary difference is related to different magnetic sources on the photosphere and corresponding large scale magnetic topologies in the corona. It should be mentioned that the CME velocity measurements are accompanied by uncertainties due to the projection effect, the instrument sensitivity and cadence, and the subjective judgement of the eruptive features.

Therefore, the evolutionary speed difference reported here should be verified in future studies.

We examined NGDC for possible microwave bursts in the obtained 6-hour time window of our events. The data are available for 9 of our events occurring after Jan. 2000. It can be seen that none of these events are associated with significant microwave enhancements, say, reaching a level greater than  $100 \text{ W m}^{-2} \cdot \text{Hz}^{-1}$ . Neither are seen considerable brightening in the EUV wavelength according to the EIT data.

Now we summarize the common observational features of the 13 events as discussed above. All these CMEs are (1) front-side, flareless, fast, and relatively-wide events, (2) accompanied by post-eruption EUV loops, yet no considerable enhancements in X-ray, EUV, and microwave data (when available), (3) originated from quiet-Sun regions related to extended magnetic structures of weak fields, (4) associated with well-developed filament eruptions. Note the first group of features is given by our event selection criteria. In the following discussion some of the above features will be demonstrated with 2 events which are selected from Group A (Event 10) and Group B (Event 2), respectively. In both events the filament eruptions, and post-CME loops and ribbons were clearly observed, microwave flux data at various frequencies are also available from Nobeyama Solar Radio Observatory (NSRO). In addition, both events are relatively close to the solar center allowing the magnetic field strength to be measured with MDI. Thus, besides demonstrating some of the above common observational features of the 13 events, the two cases are also used to measure the filament dynamics and estimate the reconnection electric fields (e.g., Qiu et al. 2002).

The first appearance times of the two CMEs in C2 were 02:30 UT and 07:02 UT, and the back-extrapolated CME start times were 02:04 UT and 06:30 UT. In Figure 3a we present the pre-eruption  $\text{H}\alpha$  images of the filaments recorded by the Mauna Loa Solar Observatory (MLSO), superposed by contours of the MDI magnetic field data with yellow (blue) colors representing positive (negative) magnetic polarities. The MDI synoptic map for CR1997 is also shown to illustrate more clearly the relative location of the filament (indicated by the red line) and the magnetic structure. One C2 difference image and the EIT data of the post-eruption loops are shown in Figures 3c and 3d. Similar data are shown in Figure 4 for Event 2 of Group B. It can be seen that the filament in Event 10 lies within an EBR region while that in Event 2 between two adjacent EBRs. Similar conclusions apply for the other events in the respective group. In both events we can observe diffusive signatures ahead of the bright CME ejecta and the deflection of nearby coronal ray structures from Figures 3c and 4c. These features have been taken as possible signatures of coronal shocks (e.g., Vourlidis et al. 2003; Sheeley et al. 2000; Feng et al. 2013). Considering both CMEs are fast, it is conceivable that coronal shocks were generated in both events.

It should be stressed that the post-eruption loops and ribbons were observed in all our events. These flare-like features can be taken as evidences of magnetic reconnection. In Figures 5 and 6 we plot the NSRO microwave fluxes at frequencies of 2 (red), 3.75 (green) and 9.4 (blue) GHz in the obtained 6-hour time window for Event 10 and Event 2, respectively. It can be seen that there were no obvious responses to the eruptions in these microwave data, as mentioned before. This

indicates a lack of efficient plasma heating and electron acceleration during the eruptions, although reconnections are involved. This statement applies to all the events with microwave data.

The Mark-IV (MK4) coronagraph (Elmore et al. 2003) observes the corona with a smaller FOV than LASCO C2. However, none of our events were well observed by MK4. Therefore, we made use of the filament motion to approximate the CME dynamics in the lower corona. Following Wang et al. (2003) and Qiu et al. (2004), we measured the positions of the filament center and top, and deduced the corresponding heights assuming a radially-outward propagation. This reduces the projection effect on the height measurement. The obtained filament heights are given in Figures 7 (Event 10) and 8 (Event 2) along with the heights of the CME front (measured by the authors). The velocities and accelerations as well as their errors were determined with the same method as used in Figures 1 and 2. The filament height measurement uncertainty is estimated to be 5 pixels of the EIT image. This already considers the errors caused by the projection effect. It can be seen that for Event 10 the maximum velocities (accelerations) of the filament and CME fronts are  $140 \text{ km s}^{-1}$  ( $0.061 \text{ km s}^{-2}$ ) and  $992 \text{ km s}^{-1}$  ( $0.073 \text{ km s}^{-2}$ ), respectively. For Event 2 the maximum velocities (accelerations) are  $136 \text{ km s}^{-1}$  ( $0.082 \text{ km s}^{-2}$ ) and  $1083 \text{ km s}^{-1}$  ( $0.112 \text{ km s}^{-2}$ ) for the filament and CME front, respectively. The vertical dashed lines in both figures represents the time at which the post-eruption ribbons appeared in the FOV and the time at which the separation stopped. These times are 02:00 (06:00) UT and 04:36 (08:05) UT for Event 10 (2). It can be seen that the filament started to rise rapidly at  $\sim 01:00$  (05:00) UT, and the CME stopped the acceleration at  $\sim 05:00$  (09:00) UT in Event 10 (2). In other words, in both events the filament rose earlier than the appearance of post-eruption ribbons, and the total acceleration time of filaments and CME fronts was considerably longer than the ribbon separation time.

Following Qiu et al. (2002, 2004) and Wang et al. (2003), we also estimated the reconnection electric field, which is given by the product of separation speeds of the EIT observed post-eruption ribbons and the magnetic field strength measured with MDI. This was done for three points along the ribbons (marked as A, B, and C in Figures 3d and 4d). The average reconnection fields are estimated to be 0.04, 0.03, 0.03  $\text{V cm}^{-1}$  for the three points with a maximum less than 0.07  $\text{V cm}^{-1}$  in Event 10. These values are 0.06, 0.04, 0.08  $\text{V cm}^{-1}$  with a maximum less than 0.1  $\text{V cm}^{-1}$  in Event 2. Nevertheless, due to the noise level of the MDI magnetic field measurement, the error of the reconnection electric field measurement is notoriously large ( $\sim 0.1 \text{ V cm}^{-1}$ ) which is actually comparable to the physical values themselves. This prevents us from getting any meaningful conclusion of the variation trend of the electric field. The only robust deduction is that the reconnection electric field remains weak during the reconnection process. This is consistent with the lack of significant emission enhancements in the X-ray, EUV, and microwave wavelength. The inferred reconnection electric field does not exceed 0.1-0.2  $\text{V cm}^{-1}$ , much weaker than the values reported in previous studies. For example, Qiu et al. (2004) reported that the maximum reconnection electric field, estimated with the same methods as that used here, was 5.8 (0.5)  $\text{V cm}^{-1}$  for a CME with an accompanying X1.6 (M1.0) flare.

### 3. Discussion

It is a core issue of CME studies regarding the release mechanism of magnetic energy in the corona. Two major mechanisms have been suggested including the ideal MHD flux rope instability and magnetic reconnection (see, e.g., Chen et al., 2007a, 2007b; Chen 2013). It is possible that in a specific event both processes contribute. Then a natural question arises: how can we determine the relative contribution of each mechanism? Observationally this is not a trivial issue to resolve due to the following limitations. (1) There is no direct technique to measure the coronal magnetic field on a daily basis, and therefore the energy involved in the eruption can not be determined directly; (2) In many events the dynamics of CMEs in the inner corona can not be observed due to the FOV limits of coronagraphs, while a major part of the CME acceleration (as well as the energy conversion) takes place there; (3) Available estimates of the CME initial acceleration, mass and kinetic energy suffer from large errors because of the instrument sensitivity and resolution, the projection effect, as well as the limitations of the plasma density inversion method. These factors make the studies of CME energetics difficult.

Theoretically, the relative contribution of the two processes can be evaluated with a numerical model of flux rope eruption as done by Chen et al. (2007a). As mentioned previously, Chen et al. found that a flux rope eruption as fast as  $1000 \text{ km s}^{-1}$  can be simulated with the ideal flux rope instability in the absence of magnetic reconnection. After reconnection sets in, the flux rope moves faster with more magnetic energy being converted into the CME kinetic energy. They compared the kinetic energy changes of the system with and without reconnections and concluded that the two magnetic energy release processes, if reconnections are invoked, can have comparable contributions to the flux rope eruption. Note that numerical resistivity was used to invoke reconnections in their model, which is believed to be several orders of magnitude larger than a physical one. Therefore, the obtained contribution of reconnection to the increase of the flux rope kinetic energy should be taken as an upper limit.

Generally speaking, the contribution of different mechanism in a specific event shall depend on the details of the global and local magnetic topologies, as well as the details of reconnections and the eruption. For the 13 events listed in Table 1, although they belong to fast CMEs with kinetic energies estimated to be considerably larger than average values, no accompanying X-ray flares were observed, neither the usual flare-related emission fluxes in the soft-X ray and microwave wavelengths showed appreciable enhancement. The reconnection electric fields estimated for two events remained lower than  $0.1 \text{ V cm}^{-1}$  during the eruption. In addition, in both events the filament rose  $\sim 1\text{h}$  earlier than the appearance of post-eruption ribbons, and the total acceleration time of filaments and CMEs was considerably longer than the time with a measurable reconnection electric field. These observational features strongly indicate that magnetic reconnections played only a minor role in accelerating the CMEs out of the corona. Considering that (1) reconnections and flux rope instabilities are the two major magnetic energy release mechanisms proposed so far, and (2) all our events correspond to well-developed filament eruptions indicating the presence of large-scale flux rope structure (e.g., Low 1996), we suggest that the flux rope instability dominates the energy



releases in our events.

The above judgement on the existence of flux ropes in the corona is mainly based on the presence of filaments. Yet, it is not possible to confirm the existence of such a coronal magnetic structure observationally as the coronal magnetic field can not be measured directly at this time. There exist other observational signatures supporting the existence of a flux rope in the corona, like the rope-like or tangled white light structures from the coronagraph observations (e.g., Dere et al. 1999), the sigmoid structure observed in the CME source (Canfield et al. 1999; McKenzie & Canfield 2008) as well as coronal cavities (e.g., Gibson et al. 2006; Riley et al. 2008). In recent studies using the high-resolution *SDO* (Solar Dynamics Observatory) data, a hot-channel structure was observed in the 131 Å wavelength (Cheng et al. 2011; Zhang et al. 2012) and interpreted as a kind of flux rope structure. According to Zhang et al. (2012) the hot channel manifested itself as a twisted structure which got untwisted to an accelerating and expanding arcade. It is obvious that the active-region hot-channel flux rope is different in thermal and magnetic properties from those quiet-Sun filament-flux rope structure discussed in the present study. It remains unknown whether and how these discrepancies of flux rope structures may affect the contributions of different energy release process.

It is useful to compare and understand why flareless fast CMEs are very different from those fast events with strong accompanying flares. The fast events with strong flares usually originate from solar active regions, while all our events are from EBRs with relatively weak fields in the quiet-Sun region. This difference of magnetic sources may be one important cause of the different characteristics of the above two types of fast CMEs. As suggested, magnetic reconnections play only a minor role in our events, whose role shall presumably become more important in those fast CMEs with strong flares. Yet, it is not possible to determine the relative contribution of reconnections and flux rope instabilities with available observations. It is also not clear whether the above two types of fast CMEs are physically different or they just represent two extremes of a broad CME distribution with similar eruption mechanism(s). This issue should be addressed in future studies.

Another interesting point is that for all our events there were no accompanying type II radio bursts according to the Radio Solar Telescope Network (RSTN) and NGDC data, neither were there associated solar energetic particle (SEP) events based on the CDAW database. As mentioned, the CMEs propagated very fast with a high possibility of driving a coronal shock. And we indeed observed in  $\sim 10$  of our events the diffusive halo structure ahead of the bright CME ejecta and the deflections of coronal streamers that were not in apparent contact with the ejecta. These phenomena are regarded as possible shock signatures (e.g., Vourlidas et al. 2003; Sheeley et al. 2000, Feng et al., 2013). In addition, among our events 7 were from the western hemisphere. This favors the propagation of energetic particles to the near-Earth space. Therefore, one natural explanation for the absence of type IIs and SEPs is that the shocks, if they existed, were not capable of accelerating electrons and ions to high enough energies.

Relevant studies indicate that efficient particle acceleration via shocks may require seed par-

ticles with enough number and energy, as well as an enhanced turbulence level. These conditions may be provided by the accompanying flare process or by preceding eruptions (e.g., Li 2012; Ding et al., 2013). With a careful examination, it was found that in 10 of the 13 events there seem no preceding eruptions that were able to strongly disturb the propagation environment of the CME in study. For the rest 3 events (Event 2, 5, and 6), preceding-CMEs were observed. This possibly indicates that preceding-CMEs are only one favorable condition for efficient particle acceleration. In summary, the above analysis implicates that the conditions of no accompanying flares and no preceding-CMEs do not favor the acceleration of energetic particles via shocks, thus provides a support to the above theories of shock particle acceleration. Of course, it is not possible to completely rule out the possibility that there were energetic particles and type IIs associated with the shock, yet not observable due to their propagation and transport effect.

#### 4. Summary

In this paper we presented a special group of fast front-side CMEs, which had no associated flares. We found that all the events were associated with filament eruptions originated either within a single EBR or between adjacent EBRs in the quiet-Sun region. During the eruption, we observed post-eruption ribbons and loops, in accordance with the standard flare picture, indicating the presence of magnetic reconnections in these events. However the following features suggest that ideal MHD instabilities of the flux rope rather than reconnections played a dominant role in the energy release process of the events. (1) No accompanying GOES X-ray flares and corresponding flux enhancements in the soft X-ray and microwave radiations were present. This means that the relevant radiations of this event were below the background emission level. (2) In two events, it was revealed that the filaments rose earlier than the appearance of post-eruption ribbons, and the total acceleration time of filaments and CME fronts was considerably longer than the time with measurable reconnection electric field that was weak in general. (3) The presence of well-developed long filaments indicated the existence of large-scale flux rope structures in the corona. These results are consistent with previous modelling results showing that a fast eruption of the flux rope can be yielded considering the ideal flux rope instabilities as the only magnetic-energy release mechanism of the eruption, and suggest that magnetic reconnection plays a less important role in accelerating CMEs in quiet Sun regions of weak magnetic field than those in active regions of strong magnetic field.

#### 5. Appendix

In this section, we present all the 23 flares reported by the National Geophysical Data Center (NGDC) (<ftp://ftp.ngdc.noaa.gov/STP/spaceweather/solar-data/>) in the 6-hour time window centered at the back-extrapolated CME start time, and determine their relevance to the CME major accelerations. These flares have been numbered in the GOES X-ray fluxes (0.1 - 0.8 nm) shown

in Figures 1 and 2. In table 2 we list the relevant information of the flares. The flare and event numbers and group identification are given in the first column. The start, peak and stop time are given in the next three columns. The last two columns are their X-ray classifications and locations, including the active region number. There are 6 flares whose source information remains unknown. Parameters listed here are taken from NGDC.

Table 2: Information of the 23 flares numbered in Figures 1 and 2.

Flare#/Event# /Group	Start Time (UT)	Peak Time (UT)	Stop Time (UT)	Class	Position (NOAA)
01/01/B	98/01/03 12:12	12:20	12:26	C3.3	No Source Info. <sup>a</sup>
02/02/B	98/06/05 04:39	04:45	04:51	C1.4	S26E43 (08232) <sup>b</sup>
03/02/B	98/06/05 06:43	06:48	06:54	B9.0	S25E45 (08232)
04/05/B	00/07/24 15:55	16:00	16:21	C2.8	S31E45 (09100)
05/06/B	02/03/02 12:55	12:59	13:03	C1.1	No Source Info. <sup>b</sup>
06/07/A	02/05/11 16:45	16:50	16:54	C2.7	S06E48 (09946) <sup>b</sup>
07/07/A	02/05/11 17:32	17:38	17:41	C3.7	S17W58 (09934) <sup>b</sup>
08/07/A	02/05/11 18:32	18:36	18:37	B9.7	S15W57 (09934) <sup>b</sup>
09/07/A	02/05/11 21:46	21:50	21:53	C1.5	No Source Info. <sup>a</sup>
10/08/A	02/07/13 08:12	08:15	08:18	C2.2	N17E35 (10030) <sup>b</sup>
11/09/A	02/08/06 15:16	15:27	15:52	C7.6	S06W66 (10057) <sup>b</sup>
12/09/A	02/08/06 20:05	20:09	20:11	C1.3	No Source Info. <sup>a</sup>
13/10/A	02/12/20 23:17	23:21	23:24	C2.0	S25W37 (10226) <sup>b</sup>
14/10/A	02/12/20 23:58	00:02	00:08	C1.7	S28W38 (10226) <sup>b</sup>
15/10/A	02/12/21 02:46	02:52	02:57	C2.4	S27W45 (10226)
16/10/A	02/12/21 03:39	03:49	03:56	C2.9	N19W19 (10229) <sup>a</sup>
17/10/A	02/12/21 04:38	04:41	04:45	C2.2	No Source Info. <sup>a</sup>
18/10/A	02/12/21 04:48	04:53	04:57	C4.6	S25W41 (10226) <sup>a</sup>
19/12/A	03/01/05 07:54	07:58	08:02	C1.0	S08E27 (10242) <sup>b</sup>
20/12/A	03/01/05 09:24	09:28	09:32	B9.2	S19W55 (10243)
21/12/A	03/01/05 11:51	11:54	11:58	C1.3	No Source Info. <sup>a</sup>
22/13/B	05/01/04 05:59	06:16	06:30	C3.3	N05W07 (10715) <sup>b</sup>
23/13/B	05/01/04 10:53	11:13	11:29	C7.3	N05W11 (10715) <sup>a</sup>

<sup>a</sup>Flares started 1 hour after the CME appearance time in LASCO C2.

<sup>b</sup>Flares ended before the apparent rise of the associated filament.

The flare-CME associations are determined via the following three steps. Firstly, flares started 1 hour after the CME appearance time in LASCO C2 are considered to be irrelevant. At this time, the CME, propagating very fast in general, should have moved to the outer corona and finished most of its acceleration. This removes 11 flares as relevant events, including 5 flares without source

information. They are indicated with a subscript ‘a’ in the table. Further examinations of the LASCO data confirmed that the CME fronts are already beyond  $8 R_{\odot}$  at the time of these flares. Secondly, flares ended before the apparent rise of the associated filament, marked with a subscript ‘b’, are also considered to be irrelevant. This removes 8 other flares including the last one with unknown source location. Last, we examined the left 4 flares (No. 3, 4, 15, and 20), and found that their X-ray emissions are only marginally beyond the background emission level, and they are from active regions not close to our CME sources as verified by the EIT imagings. Therefore, neither are they considered to be relevant to our study.

We thank the anonymous referee for his/her constructive comments that improved this paper. We are grateful to Dr. Guangli Huang, Jun Zhang, Guiping Zhou, and Xin Cheng for their comments and suggestions. This work was supported by the 973 program 2012CB825601, NNSFC grants 41104113, 41274177, and 41274175. H. Q. Song was also supported by the Natural Science Foundation of Shandong Province ZR2010DQ016, and the Independent Innovation Foundation of Shandong University 2010ZRYB001. We acknowledge the use of the CDAW CME catalog, which is generated and maintained at the CDAW Data Center by NASA and the Catholic University of America in cooperation with the Naval Research Laboratory. SOHO is a project of international cooperation between ESA and NASA. We are also grateful to the NSRO, MLSO, BBSO, KSO, and YNAO teams for making their data available to us.

## REFERENCES

- Brueckner, G. E., Howard, R. A., Koomen, M. J., et al. 1995, *Sol. Phys.*, 162, 357
- Canfield, R. C., Hudson, H. S., & McKenzie, D. E. 1999, *Geophys. Res. Lett.*, 26, 627
- Carmichael, H. 1964, in *NASA Special Publication, Vol. 50, The Physics of Solar Flares*, ed. W. N. Hess (Washington, DC: NASA), 451
- Chen, J., & Krall, J. 2003, *J. Geophys. Res.*, 108, 1410
- Chen, P. F. 2011, *Living Rev. Solar Phys.*, 8, 1
- Chen, Y. 2013, *Chin Sci Bull.*, 58, 1599
- Chen, Y., Li, G. Q., & Hu, Y. Q. 2006, *ApJ*, 649, 1093
- Chen, Y., Hu, Y. Q., & Sun, S. J. 2007a, *ApJ*, 665, 1421
- Chen, Y., Hu, Y. Q., & Xia, L. D. 2007b, *Adv. Space Res.*, 40, 1780
- Cheng, X., Zhang, J., Liu, Y., & Ding, M. D. 2011, *ApJ*, 732, L25
- Delaboudiniere, J. P., Artzner, G. E., Brunaud, J., et al. 1995, *Sol. Phys.*, 162, 291

- Dere, K. P., Brueckner, G. E., Howard, R. A., Michels, D. J., & Delaboudiniere, J. P. 1999, *ApJ*, 516, 465
- Ding, L. G., Jiang, Y., Zhao, L. L., & Li, G. 2013, *ApJ*, 763, 30
- Elmore, D. F., Burkepile, J. T., Darnell, J. A., Lecinski, A. R., & Stanger, A. L. 2003, *Proc. SPIE*, 4843, 66
- Fan, Y. H., & Gibson, S. E., 2007, *ApJ*, 668, 1232
- Feng, S. W., Chen, Y., Kong, X. L., Li, G., Song, H. Q., Feng, X. S., and Guo F. 2013, *ApJ*, 767, 29
- Forbes, T. G., & Isenberg, P. A. 1991, *ApJ*, 373, 294
- Forbes, T. G., & Priest, E. R. 1995, *ApJ*, 446, 377
- Gibson, S. E., Foster, D., Burkepile, J., de Toma, G., & Stanger, A. 2006, *ApJ*, 641, 590
- Gopalswamy, N., Yashiro, S., Michalek, G. et al. 2009, *Earth Moon Planet*, 104, 295
- Gosling, J. T., Hildner, E., Macquees, R. M. et al. 1976, *Sol. Phys.*, 48, 389
- Harrison, R. A. 1995, *A&A*, 304, 585
- Hirayama, T. 1974, *Sol. Phys.*, 34, 323
- Hu, Y. Q., Li, G. Q., & Xing, X. Y. 2003, *J. Geophys. Res.*, 108, 1072
- Hundhausen, A. J. 1997, *An Introduction, Coronal Mass Ejections*, AGU Geophysical Monograph 99, (eds) Crooker, N. et al., Washington D. C.
- Isenberg, P. A., Forbse, T. G., & Demoulin, P. 1993, *ApJ*, 417, 368
- Kliem, B., & Török, T. 2006, *Phys. Rev. Lett.*, 96, 255002
- Kopp, R. A., & Pneuman, G. W. 1976, *Sol. Phys.*, 50, 85
- Li, G., Moore, R., Mewaldt, R. A., Zhao, L., & Labrador, A. W. 2012, *Space Sci. Rev.*, 171, 141
- Low, B. C. 1996, *Sol. Phys.*, 167, 217
- Maričić, D., Vršnak, B., Stanger, A. L., et al. 2007, *Sol. Phys.*, 241, 99
- McKenzie, D. E., & Canfield, R. C. 2008, *A&A*, 481, L65
- Olmedo, D. & Zhang, J. 2010, *ApJ*, 718, 433
- Priest, E. R., & Forbes, T. G. 1990, *Sol. Phys.*, 126, 319

- Qiu, J., Hu, Q., Howard, T. A., & Yurchyshyn, V. B. 2007, *ApJ*, 659, 758
- Qiu, J., Lee, J., Gary, D. E., & Wang, H. M. 2002, *ApJ*, 565, 1335
- Qiu, J., Wang, H. M., Cheng, C. Z., & Gary, D. E. 2004, *ApJ*, 604, 900
- Rachmeler, L. A., Deforest, C. E., & Kankelborg, C. C. 2009, *ApJ*, 693, 1431
- Riley, P., Lionello, R., Mikić, Z., & Linker, J. 2008, *ApJ*, 672, 1221
- Scherrer, P. H., Bogart, R. S., Bush, R. I., et al. 1995, *Sol. Phys.*, 162, 129
- Sheeley Jr, N. R., Walters, J. H., Wang, Y. M., & Howard, R. A. 1999, *J. Geophys. Res.*, 104, 24739
- Sheeley, Jr, N. R., Hakala, W. N., & Wang, Y. M. 2000, *J. Geophys. Res.*, 105, 5081
- Sturrock, P. A. 1966, *Nature*, 211, 695
- Van Tend, W., & Kuperus, M. 1978, *Sol. Phys.*, 59, 115
- Vourlidis, A., Wu, S. T., Wang, A. H., Subramanian, P., & Howard, R. A., 2003, *ApJ*, 598, 1392
- Vršnak, B., Sudar, D., & Ruždjak, D. 2005, *A&A*, 435, 1149
- Wang, H. M., Qiu, J., Jing, J., & Zhang, H. Q. 2003, *ApJ*, 593, 564
- Wang, Y. M., & Zhang, J. 2007, *ApJ*, 665, 1428
- Webb, D. F., & Howard, T. A. 2012, *Living Rev. Solar Phys.* 9, 3
- Yashiro, S., Gopalswamy, N., Akiyama, S., Michalek, G., & Howard, R. A. 2005, *J. Geophys. Res.*, 110, A12S05
- Yashiro, S., Gopalswamy, N., Michalek, G., & Howard, R. A. 2002, *BAAS*, 34, 695
- Yeh, C. T., Ding, M. D., & Chen, P. F., 2005, *Sol. Phys.*, 229, 313
- Zhang, J., Cheng, X., & Ding, M. D. 2012, *Nature Communications*, 3, 747
- Zhang, J., & Dere K. P. 2006, *ApJ*, 649, 1100
- Zhang, J. Dere, K. P., Howard, R. A., Kundu, M. R., & White, S. M. 2001, *ApJ*, 559, 452
- Zhou, G. P., Wang, J. X., & Zhang, J. 2006, *A&A*, 445, 1133
- Zhou, G. P., Wang, Y. M., & Wang, J. X. 2005, *Advances in Space Res.*, 38, 466

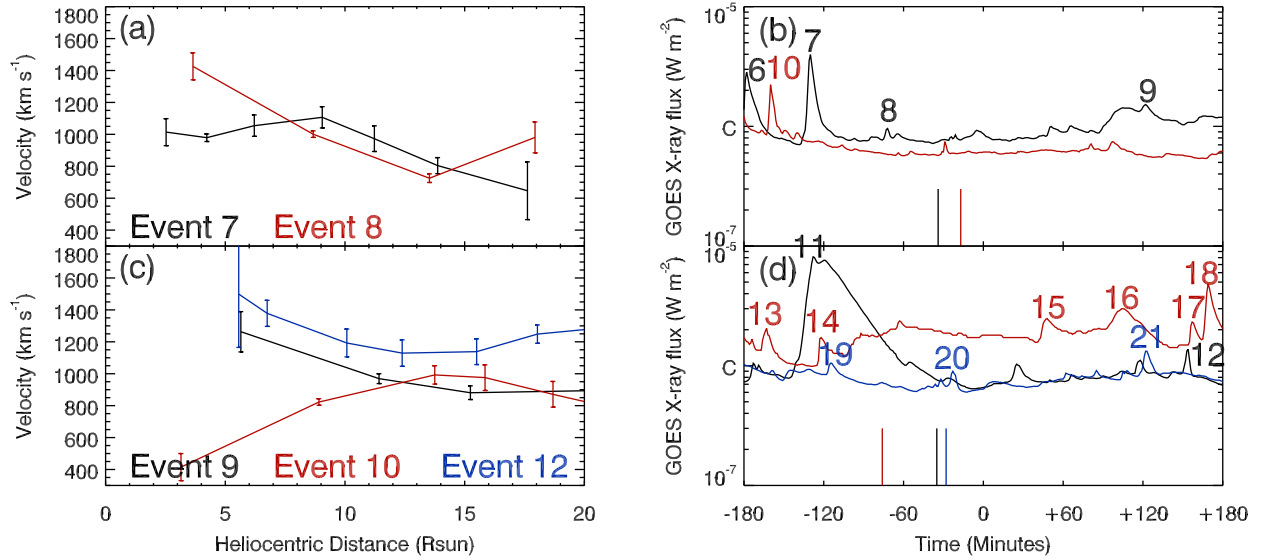


Fig. 1.— CME speeds and GOES X-ray fluxes for the 5 Group A events listed in Table 1. Left panels are the radial variation of the projected speeds of CMEs measured with the LASCO C2 and C3 data. Right panels are the corresponding GOES X-ray (0.1 - 0.8 nm) fluxes in the 6-hour time window centered at the back-extrapolated CME start time. Flares given by NGDC in the time window are numbered, whose information is listed in Table 2 of the Appendix. Colors are used to represent different CME events. The vertical lines in the right panels indicate the time the associated filaments start to rise noticeably. (A color version of this figure is available in the online journal.)

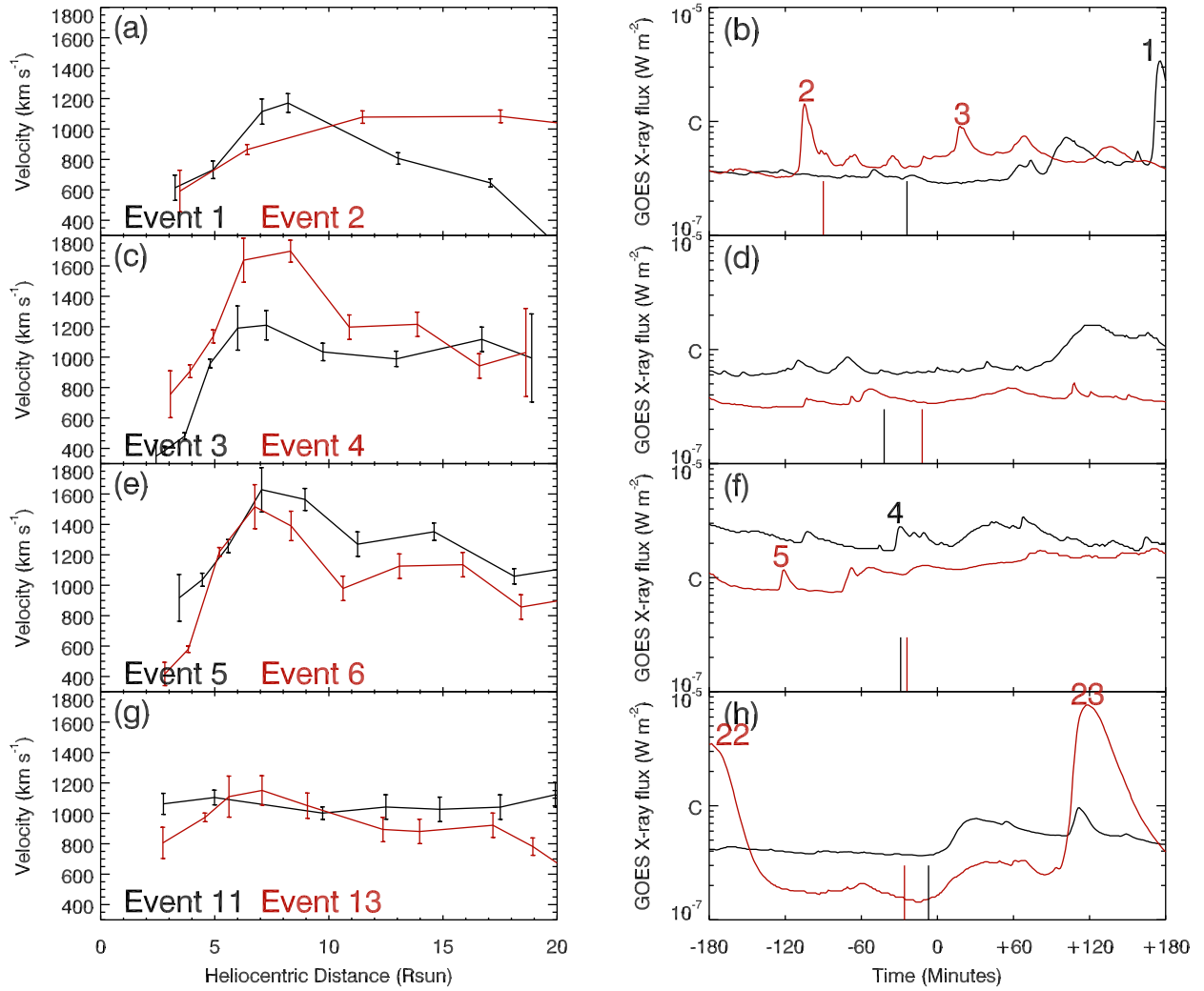


Fig. 2.— Same as Figure 1 but for the 8 Group B events listed in Table 1. (A color version of this figure is available in the online journal.)



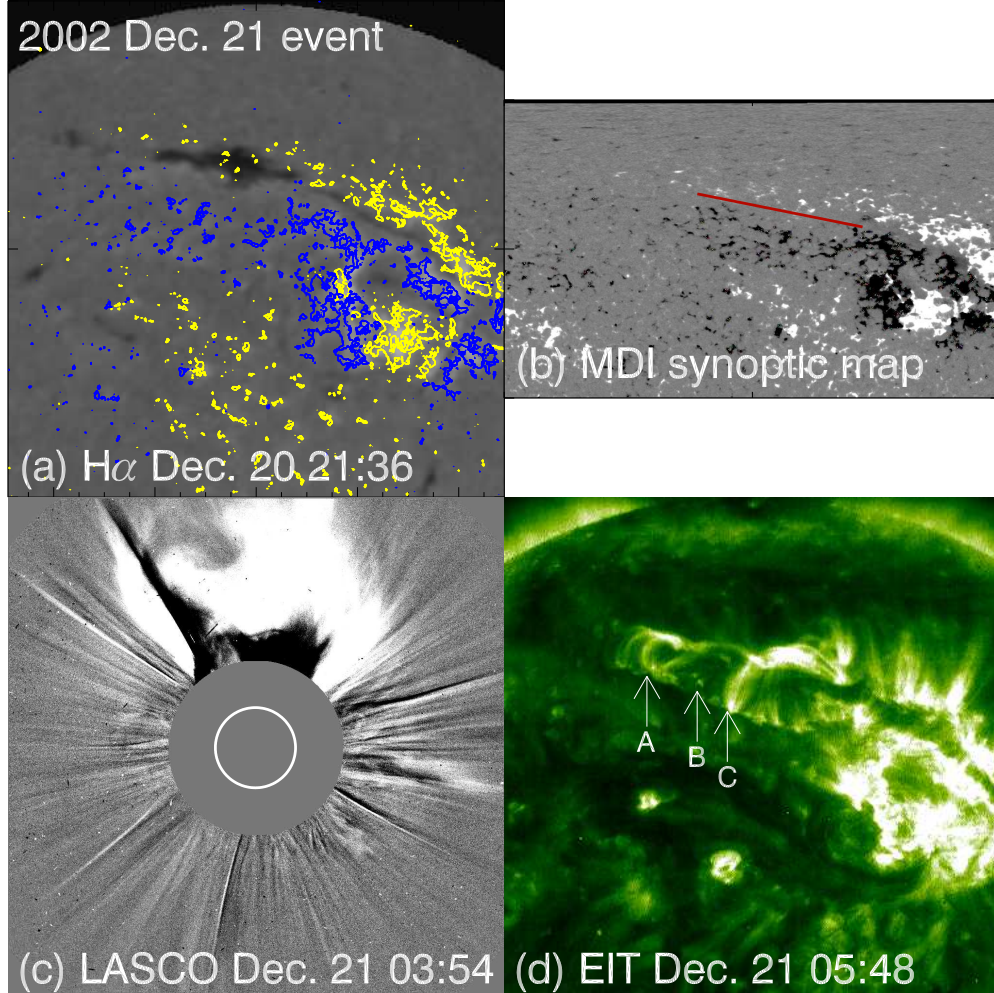


Fig. 3.— Observations of the 2002 Dec. 21 event (Event 10) in Group A. (a) The pre-eruption  $H\alpha$  images recorded by the MLSO, superposed by contours of the MDI magnetic field data (20:48 UT on the same day) with yellow (blue) colors representing positive (negative) magnetic polarities. (b) MDI synoptic map for CR1997 with a FOV of  $[0, 90]$  for the latitude and  $[30, 120]$  for the longitude, the red line indicates the location of the relevant filament. (c) The LASCO C2 difference image of the CME. (d) the EIT data of the post-eruption loops. The FOVs of (a) and (d) are identical taken to be  $[-0.5 R_{\odot}, 0.5 R_{\odot}]$  for the horizontal axis and  $[0, 1 R_{\odot}]$  for the vertical axis. Three points in (d) along the expanding loops are marked for reconnection election field measurements. (Animations of the EIT data and a color version of this figure is available in the online journal.)

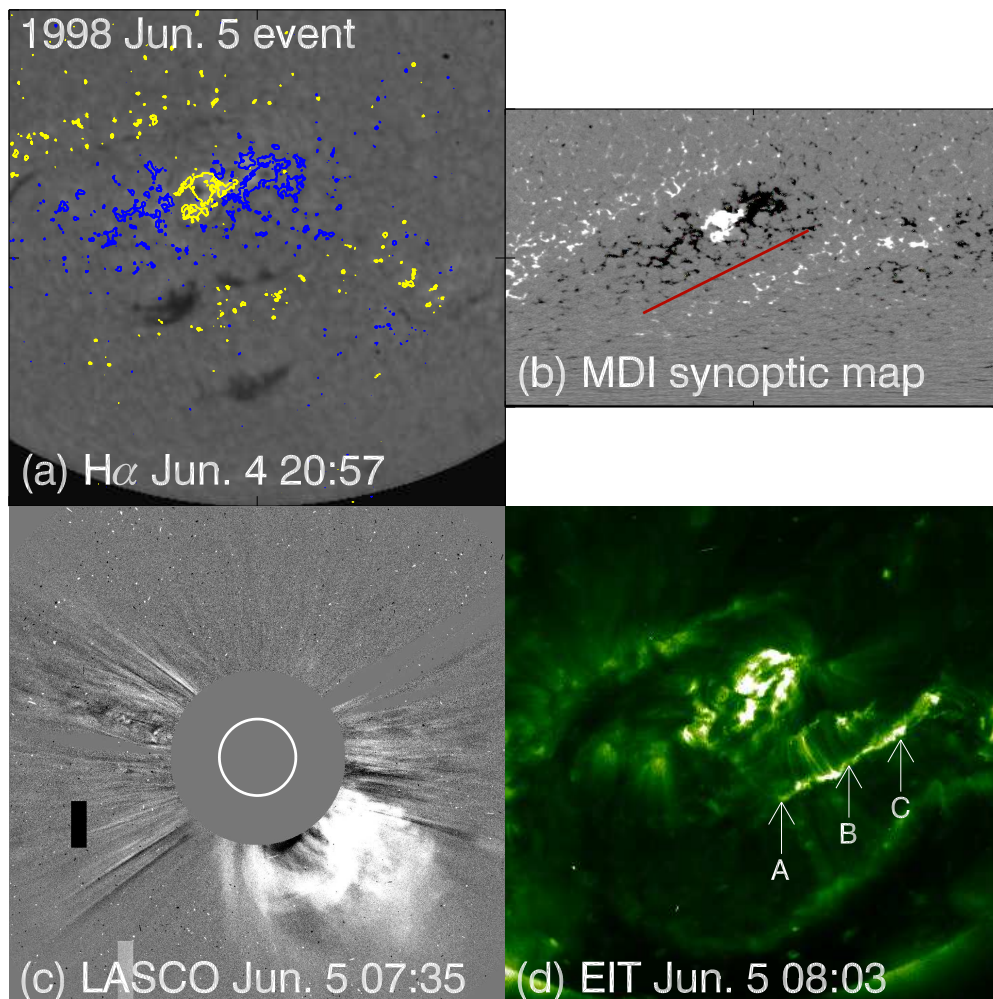


Fig. 4.— Observations of the 1998 Jun. 5 event (Event 2) in Group A. (a) The pre-eruption  $H\alpha$  images recorded by the MLSO, superposed by contours of the MDI magnetic field data (20:48 UT on the same day) with yellow (blue) colors representing positive (negative) magnetic polarities. (b) MDI synoptic map for CR1936 with a FOV of  $[-90, 0]$  for the latitude and  $[0, 90]$  for the longitude, the red line indicates the location of the relevant filament. (c) The LASCO C2 difference image of the CME. (d) the EIT data of the post-eruption loops. The FOVs of (a) and (d) are identical taken to be  $[-0.5 R_{\odot}, 0.5 R_{\odot}]$  for the horizontal axis and  $[-1, 0 R_{\odot}]$  for the vertical axis. Three points in (d) along the expanding loops are marked for reconnection election field measurements. (Animations of the EIT data and a color version of this figure is available in the online journal.)

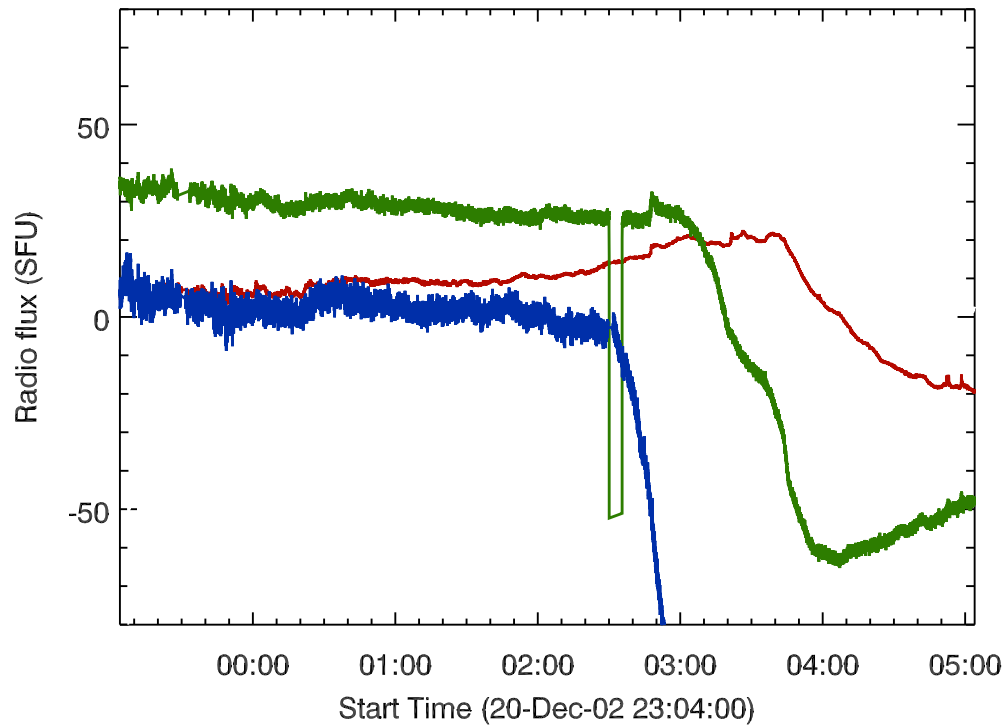


Fig. 5.— The NSRO microwave fluxes at frequencies of 2 (red), 3.75 (green) and 9.4 (blue) GHz. The center of the 6-hour time window is the estimated CME start time. (A color version of this figure is available in the online journal.)

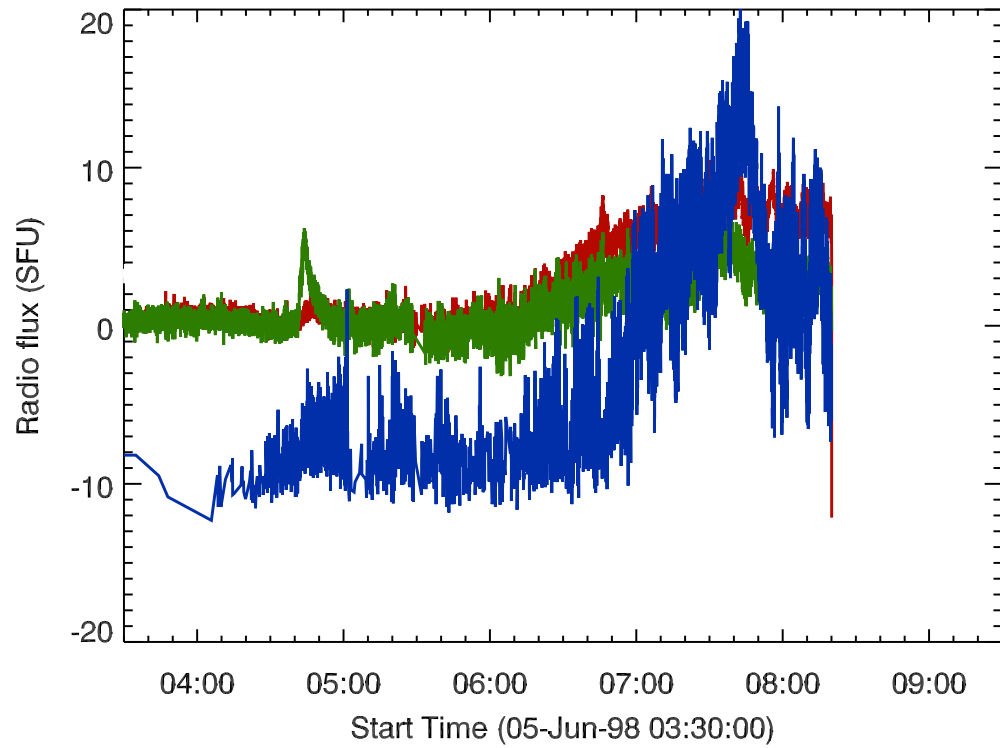


Fig. 6.— The NSRO microwave fluxes at frequencies of 2 (red), 3.75 (green) and 9.4 (blue) GHz. The center of the 6-hour time window is the estimated CME start time. (A color version of this figure is available in the online journal.)

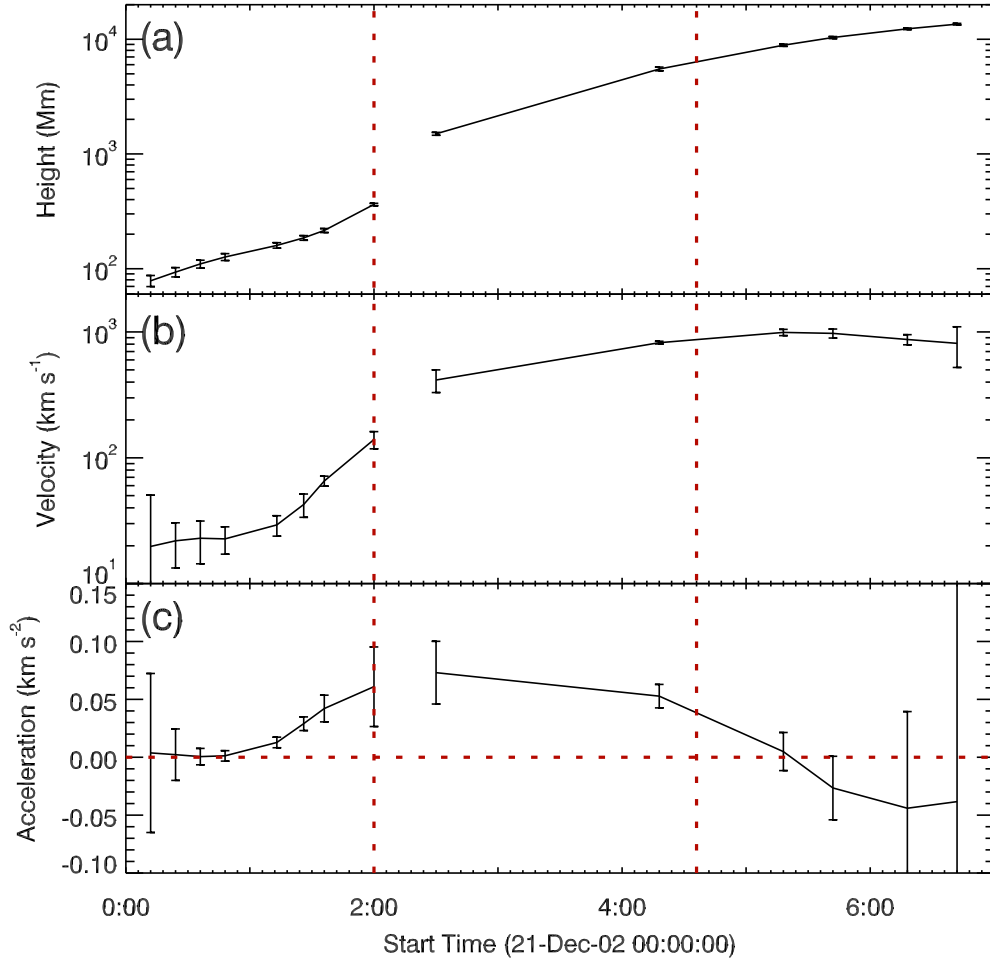


Fig. 7.— Heights, velocities, and accelerations of the filaments and CME fronts for the 2002 Dec. 21 event (Event 10) in Group A. See text for details. The vertical dashed lines indicate the time at which the post-eruption ribbons appear and the time at which they stop separating from each other. The horizontal line depicts the zero acceleration. (A color version of this figure are available in the online journal.)

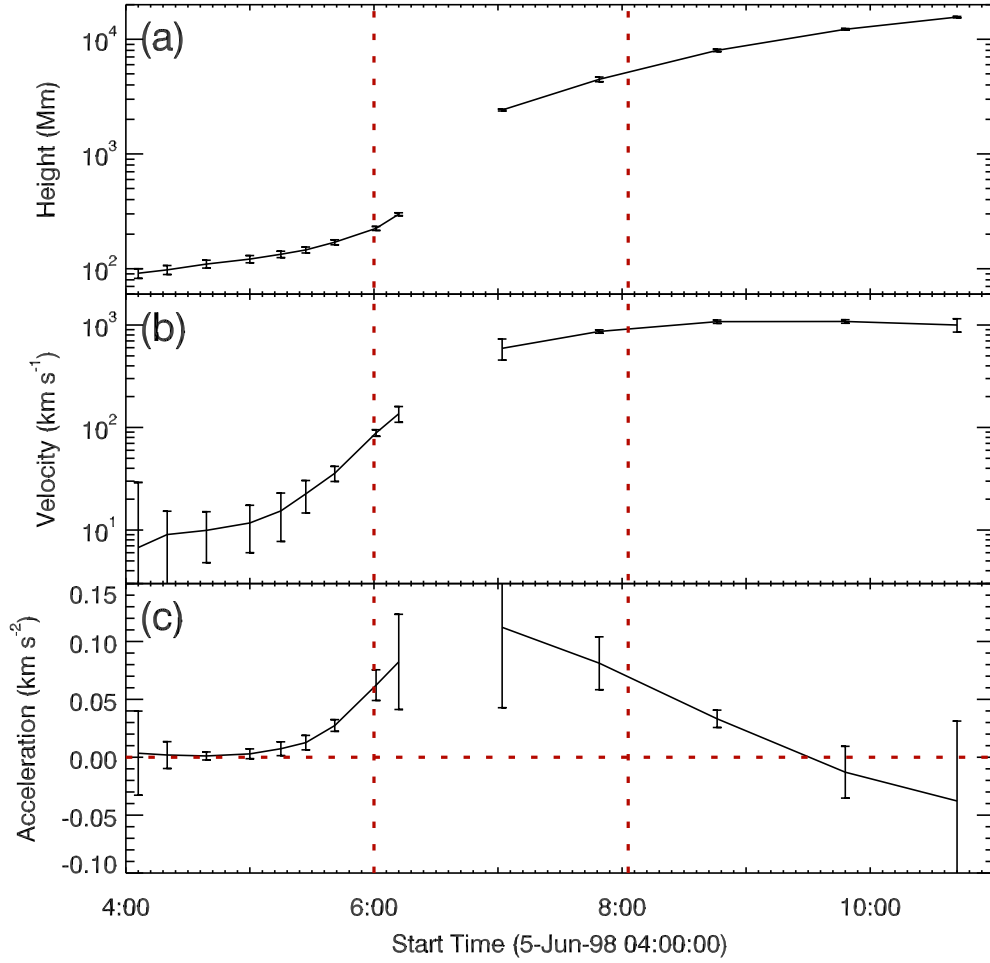


Fig. 8.— Heights, velocities, and accelerations of the filaments and CME fronts for the 2002 Dec. 21 event (Event 10) in Group A. See text for details. The vertical dashed lines indicate the time at which the post-eruption ribbons appear and the time at which they stop separating from each other. The horizontal line depicts the zero acceleration. (A color version of this figure are available in the online journal.)